



**HAL**  
open science

## Automatic segmentation methods for liver and hepatic vessels from CT and MRI volumes, applied to the Couinaud scheme

Marie-Ange Lebre, Antoine Vacavant, Manuel Grand-Brochier, Hugo Rositi, Armand Abergel, Pascal Chabrot, Benoit Magnin

### ► To cite this version:

Marie-Ange Lebre, Antoine Vacavant, Manuel Grand-Brochier, Hugo Rositi, Armand Abergel, et al.. Automatic segmentation methods for liver and hepatic vessels from CT and MRI volumes, applied to the Couinaud scheme. *Computers in Biology and Medicine*, 2019, 10.1016/j.compbiomed.2019.04.014 . hal-02121382

**HAL Id: hal-02121382**

**<https://hal.science/hal-02121382>**

Submitted on 25 Oct 2021

**HAL** is a multi-disciplinary open access archive for the deposit and dissemination of scientific research documents, whether they are published or not. The documents may come from teaching and research institutions in France or abroad, or from public or private research centers.

L'archive ouverte pluridisciplinaire **HAL**, est destinée au dépôt et à la diffusion de documents scientifiques de niveau recherche, publiés ou non, émanant des établissements d'enseignement et de recherche français ou étrangers, des laboratoires publics ou privés.



Distributed under a Creative Commons Attribution - NonCommercial 4.0 International License

# Automatic segmentation methods for liver and hepatic vessels from CT and MRI volumes, applied to the Couinaud scheme\*

Marie-Ange Lebre<sup>a</sup>, Antoine Vacavant<sup>a</sup>, Manuel Grand-Brochier<sup>a</sup>, Hugo Rositi<sup>a</sup>, Armand Abergel<sup>b</sup>, Pascal Chabrot<sup>b</sup>, Benoît Magnin<sup>b</sup>

<sup>a</sup>Université Clermont Auvergne, CNRS, SIGMA Clermont, Institut Pascal, F-63000 Clermont-Ferrand, France

<sup>b</sup>Université Clermont Auvergne, CHU Clermont-Ferrand, CNRS, SIGMA Clermont, Institut Pascal, F-63000 Clermont-Ferrand, France

## Abstract

**Background:** Proper segmentation of the liver from medical images is critical for computer-assisted diagnosis, therapy and surgical planning. Knowledge of its vascular structure allows division of the liver into eight functionally independent segments, each with its own vascular inflow, known as the Couinaud scheme. Couinaud's description is the most widely used classification, since it is well-suited for surgery and accurate for the localization of lesions. However, automatic segmentation of the liver and its vascular structure to construct the Couinaud scheme remains a challenging task.

**Methods:** We present a complete framework to obtain Couinaud's classification in three main steps; first, we propose a model-based liver segmentation, then a vascular segmentation based on a skeleton process, and finally, the construction of the eight independent liver segments. Our algorithms are automatic and allow 3D visualizations.

**Results:** We validate these algorithms on various databases with different imaging modalities (Magnetic Resonance Imaging (MRI) and Computed Tomography (CT)). Experimental results are presented on diseased livers, which pose complex challenges because both the overall organ shape and the vessels can be severely deformed. A mean DICE score of 0.915 is obtained for the liver segmentation, and an average accuracy of 0.98 for the vascular network. Finally, we present an evaluation of our method for performing the Couinaud segmentation thanks to medical reports with promising results.

**Conclusions:** We were able to automatically reconstruct 3-D volumes of the liver and its vessels on MRI and CT scans. Our goal is to develop an improved method to help radiologists with tumor localization.

**Keywords:** Medical Imaging, Liver Segmentation, Vessel Segmentation, Couinaud, CT and MRI volumes.

## 1. Introduction

Medical imaging systems such as Magnetic Resonance Imaging (MRI) and Computed Tomography (CT) provide useful information on the liver. Extraction of the organ and its vessels from images is essential for analysing disease and planning surgical operations. A scheme developed by Couinaud allows the division of the liver into eight functionally independent segments by identification of the main blood vessels (Figure 1).

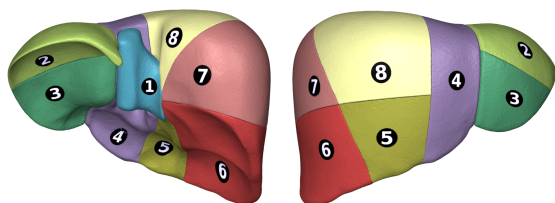


Figure 1: Illustration of the Couinaud segments. Image from [1]

This analysis is most frequently performed by a radiologist

\*This research has been supported by Région Auvergne with the grant "Nouveau chercheur" 1440NCAA and French National Agency for Research (ANR) with the reference ANR-18-CE45-0018 (R-Vessel-X project).

via visual inspection and manual segmentation. It is a time-consuming task, performed slice-by-slice, and the result depends on the skill and experience of the medical expert performing it. Moreover, segmentation is arduous because of noise, overlapping fuzzy contours, highly variable shapes and appearances, low contrast and complex backgrounds (the presence of other organs and tissues with similar intensities and shapes) [2]. To obtain the Couinaud segmentation, the liver must first be segmented, and then its vascular structure defined. Three main types of method are used for liver segmentation: classification, active contour detection, and model-based methods. Classification methods consist of grouping individual components of the image such as pixels or sub-images and exploiting their similarities as region-growing methods [3, 4], histograms with thresholds [5], voxel classification algorithms [6], and graph cuts [7]. They often lead to over-segmentation. Conversely, contour approaches seek dissimilarities [8, 9, 10, 11]. Model-based methods can be statistical or supported by an atlas [12, 13, 14]. Among these statistical models, the active appearance model (AAM) [15] and active shape model (ASM) [16, 17, 18, 19] have been widely used as high-level techniques in computer vision and image processing [20, 21]. Statistical models based on appearance or shape are parametric; thus, they require good initialization conditions and optimization of the parameters to obtain proper convergence.

For segmentation of the vascular structure of the liver, the most popular vessel enhancement filters used by the community are based on analysis of the Hessian matrix [22, 23, 24]. And their combined use brings improved results [25, 26, 27]. Morphological filters are also developed by ranking the orientation responses of path operators (RORPO) [28], an efficient tubular structure detection filter based on morphological path operators [29]. Some studies are based on region-growing or level-set methods [30, 31], and centerline extraction is also used [32, 33]. A few methods combine tubular objects into connected networks via skeletonization [34, 35].

Regardless of the approach used, most studies that present the Couinaud scheme propose a complete method, with the segmentation of the liver, its vessels and the anatomical segments. Oliveira *et al.* [30] use a deformable model with level sets for the liver, a region-growing method for vessels and built-in anatomical knowledge used to construct four planes, splitting the liver into the Couinaud regions. Chen *et al.* [36] propose a vessel-tree-based liver annotation method. A thinning algorithm allows users to obtain a spatial skeleton of liver vessels and a hierarchical vascular tree is constructed to divide the liver. Selle *et al.* [37] present a method for semi-automatic contour selection for liver segmentation, using a region-growing approach for the vessels and graph analysis for identification of the eight segments. Huang *et al.* [38] propose a method based on 3-D thinning, vascular tree pruning, classification and projection. Soler *et al.* [39] have developed a computer-assisted surgical procedure based on patient-specific geometrical and anatomical modeling. They show that Couinaud’s segmentation is not perfect, and describe some of its limitations; however, they agree it is the most widely used classification for surgery planning.

It is important to note that most researchers who work on the liver and its components present their results on CT images; few studies on MRI exist, though the latter modality is a subject of substantial interest for routine clinical oncology and diagnosis due to its superior soft tissue contrast and the lack of radiation exposure. In this study, we propose a complete automatic framework to obtain the Couinaud scheme from medical images acquired with different modalities—MRI and CT—and from patients with various degrees of progression of liver disease. First, we propose a robust, generic and efficient automatic segmentation algorithm using a model based on liver shape variability to construct a 3-D representation of any patient’s liver. Then, we introduce a 3-D automatic method based on cooperation the processes of between segmentation and skeletonization, with detection of the main centerlines of the vascular structure. At this step, the quality of the vessel segmentation is highly dependent on the pathological state of the liver. Indeed, the vessels of a healthy liver are more visible those of a patient with cirrhosis due to decreased liver function [40] and advanced cirrhosis results in a variation of the volumes of some segments and irregular borders, rendering it a challenging task. Finally, the skeleton obtained from the vascular structure allows us to produce the Couinaud segmentation.

The paper is organized as follows: Section 2 describes the complete framework, from liver segmentation to the Couinaud

scheme by way of the vascular network extraction. Section 3 presents the experimental setup, evaluation framework and results, first for the liver segmentation, then the vascular network extraction, and finally, we introduce a new measure for the Couinaud scheme. We present our conclusions in Section 4.

## 2. Methods

In the following three sections we describe the 3-D segmentation methods. We begin with liver segmentation, followed by extraction of the vascular network, and finally, we present the method to obtain the Couinaud scheme. Our methods are automatic and work on CT and MRI volumes.

To help understand the complete method, we present a table summarizing the annotations used throughout the article. The parameterization is explained in the results Section (Section 3).

Notations	Definitions
$M_{j \in \{1, m\}}$	Manual liver segmentation from available dataset (IRCAD, SLIVER, Shape 2015)
$BB$	Mean bounding box of all $M_{j \in \{1, m\}}$
$GV$	Mean 3-D gravity center of all $M_{j \in \{1, m\}}$
$\sigma_M$	Variability of segmented images
$L_M$	Set of voxels that belong to the liver in $M$
$Card(L_M)$	Cardinality of $L_M$
$S_k, k \in \{1, 4\}$	Liver sets according to the variability
$\mathbb{M}_k = \bar{M}_{j \in \{1, m_k\}}$	Mean volume constructed with each set $S_k$
$P_{j \in \{1, p\}}$	Medical images of a patient (CT or MRI)
$P_I, I \in \{1, p\}$	Slice $I$ with the largest surface of the liver
$\bar{M}_{J_1}, J_1 \in \{1, m_k\}$	Slice with the maximum binary area in the shape model $\mathbb{M}_k$
$R(\cdot)$	Resolution of an image
$\gamma_1$	Fixed percentage chosen on the shape model to select pixels on $P_I$
$P_{\bar{I}}$	Image obtained thanks to $\gamma_1$ applied on $P_I$
$\mu$	Mean value of the pixel intensity distribution of $P_{\bar{I}}$
$\delta$	Standard deviation of the pixel intensity distribution of $P_{\bar{I}}$
$\kappa(\delta)$	Function for the normality test for the first thresholding
$n_{it1}$	Number of iterations of the anisotropic diffusion filter
$ts$	Time step of the anisotropic diffusion filter
$\xi$	Conductance of the anisotropic diffusion filter
$P'_{j \in \{1, p\}}$	Volume of the patient after thresholding, anisotropic diffusion filter and gradient magnitude computation
$\gamma_2$	Fixed percentage chosen on the shape model to select pixels on $P'_{j \in \{1, p\}}$
$BP'_{j \in \{1, p\}}$	Binarization result after the used of $\gamma_2$
$MP_{j \in \{1, p\}}$	Final binary mask: result of our liver segmentation

Table 1: Annotations used for the liver segmentation method (Section 2.1)

Notations	Definitions
$I$	3-D liver segmented on medical exam
$\sigma$	To choose the scale of the detected structure for Sato's filter
$\alpha_1$	To approach the tubular structure for Sato's filter
$\alpha_2$	To recover non-homogenous contrast for Sato's filter
$I_s^1$	Result of Sato's filter on $I$ with a first set of parameters on $I$
$C_{k \in \{1, q\}}$	$q$ components detected on $I_s^1$
$l_k, k \in \{1, q\}$	Centerline of a component $C_k$
$n =  l_k $	Number of voxel of $l_k$
$\mathbf{b}_k$	Direction vector at the beginning of $l_k$
$\mathbf{e}_k$	Direction vector at the end of $l_k$
$\lambda$	Number of voxels separating the long centerlines from the short
$l_k[j]$	Voxel of $l_k$ at position $j \in \{1, n\}$
$E_{k,l}$	Extended centerline between $C_k$ and $C_l$
$ E_{k,l} $	Number of voxel of $E_{k,l}$
$I_s^1[i], i \in \{1,  E_{k,l} \}$	Intensity of each voxel of $E_{k,l}$ in $I_s^1$
$I_s^2$	Result of Sato's filter on $I$ with a second set of parameter
$\max(I_s^j), j \in \{1, 2\}$	Maximal intensity on $I_s^j$
$r_j, j \in \{1, 2\}$	Rates of intensity of $E_{k,l}$ on each $I_s^j$
$t \in [0, 1]$	Condition on the intensity rates $r_j, j \in \{1, 2\}$
$\beta$	Angle formed by $E_{k,l}$ and $C_l$
$\omega_1, \omega_2 \in [0, 1]$	Conditions on the angle $\beta$ between two components
$n_{it2}$	Limitation of the size of the centerline extension
$S_{partial}$	Partial skeleton obtained by our algorithm
$I_R$	RORPO applied on $I$
$L_{min}$	Minimal path length to detect (parameter of RORPO)
$f$	Geometric sequence of scales (parameter of RORPO)
$n_R$	Number of scales (parameter of RORPO)
$L_{n_R}$	Path length to detect (parameter of RORPO)

Table 2: Annotations used for the vessels segmentation method (Section 2.2)

## 2.1. Liver

Our segmentation of the liver is based on a model of its shape variability; its construction is described in this section.

### 2.1.1. Construction of the shape model

The shape model is constructed with data from 68 manually segmented livers these are noted  $M_{j \in \{1, m\}}$ , with  $m$  the number of slice for each volume  $M$ . They come from three different sources: Shape 2015, IRCAD and SLIVER [41, 42, 43]. On all of the binary images, we proceed using 3-D cubic interpolation with a 1-mm voxel size to obtain uniform volumes. We construct a bounding box,  $BB$ , with the mean bounding box of

the volumes, and the mean 3-D gravity center,  $GV$ . We align the gravity center of each volume with  $GV$ . We then define the variability of segmented images,  $\sigma_M$ , as the percentage of voxels measured outside the  $BB$  that belong to the liver:

$$\sigma_M = \frac{Card(L_M \setminus BB)}{Card(L_M)} \times 100 \quad (1)$$

$L_M$  is the set of voxels that belong to the liver in  $M_{j \in \{1, m\}}$ , and  $Card(L_M)$  its cardinality. Thus,  $L_M \setminus BB$  represents voxels that belong to the liver but are measured outside  $BB$ . Then, we construct four liver sets,  $S_k = \{M_{j \in \{1, m\}}\}_k$ , with  $k \in \{1, 4\}$ :

$$\begin{aligned} S_1 &= \{M_{j \in \{1, m\}}, 0\% \leq \sigma_M < 2\%\} \\ S_2 &= \{M_{j \in \{1, m\}}, 2\% \leq \sigma_M < 6\%\} \\ S_3 &= \{M_{j \in \{1, m\}}, 6\% \leq \sigma_M < 8\%\} \\ S_4 &= \{M_{j \in \{1, m\}}, \sigma_M \geq 8\%\} \end{aligned} \quad (2)$$

$S_1$  gathers the smallest livers,  $S_2$  and  $S_3$  represent standard livers, and  $S_4$  those livers bigger than  $BB$ . In each set  $S_k$ , we construct for each 2-D slice a probability map for the liver's presence. We obtain one volume for each  $S_k$ , denoted by  $\mathbb{M}_k = \bar{M}_{j \in \{1, m_k\}}$ . A pixel value  $\bar{M}(s, t) \in [0, 1]$  in a  $j$ -slice is defined by:

$$\bar{M}(s, t) = \frac{1}{m_k} \sum_{n=1}^{m_k} M(s, t), \quad (3)$$

with  $m_k = \max\{m, M_{j \in \{1, m\}} \in S_k\}$ .

Shape models are built using 68 manual segmentations. We obtain a probability map that reflects a standard position of the liver, and employ a rigid alignment to preserve invariants of pose that allows us to account for different patient positions.

### 2.1.2. Segmentation

Let  $P_{j \in \{1, p\}}$ , with  $p$  the number of slice of the volume, represent the CT or MRI images of a patient. The box  $BB$  provides an approximate position of the liver within the volume, so after a cubic interpolation (1 mm voxel size), we crop the volume on  $P_{j \in \{1, p\}}$ . In this new volume, many pixels belong to the liver and have similar intensities. So, using the intensity histogram with the highest peak, we find the slice with the largest liver surface,  $P_I, I \in \{1, p\}$ . Then, we find the slice  $\bar{M}_{J_1}$  with  $J_1 \in \{1, m_1\}$  with the maximum binary area of the first shape model  $\mathbb{M}_1$ . We note  $R(\bar{M}_{J_1})$ , the resolution of this image, and  $R(P_I)$ , the resolution of the image  $P_I$ . If the condition

$$R(P_I) \leq R(\bar{M}_{J_k} \in \mathbb{M}_k) \quad (4)$$

is false, the shape model  $\mathbb{M}_k = \mathbb{M}_1$  is too small, so we test a larger value of  $k$ :  $k + 1$ . Once an appropriate value of  $k$  is chosen, we apply  $\bar{M}_{J_k}$  as a mask on  $P_I$  by considering pixels with a probability higher than a fixed percentage  $\gamma_1$  on the shape model. The image obtained is then denoted by  $P_{\bar{J}}$ . We consider

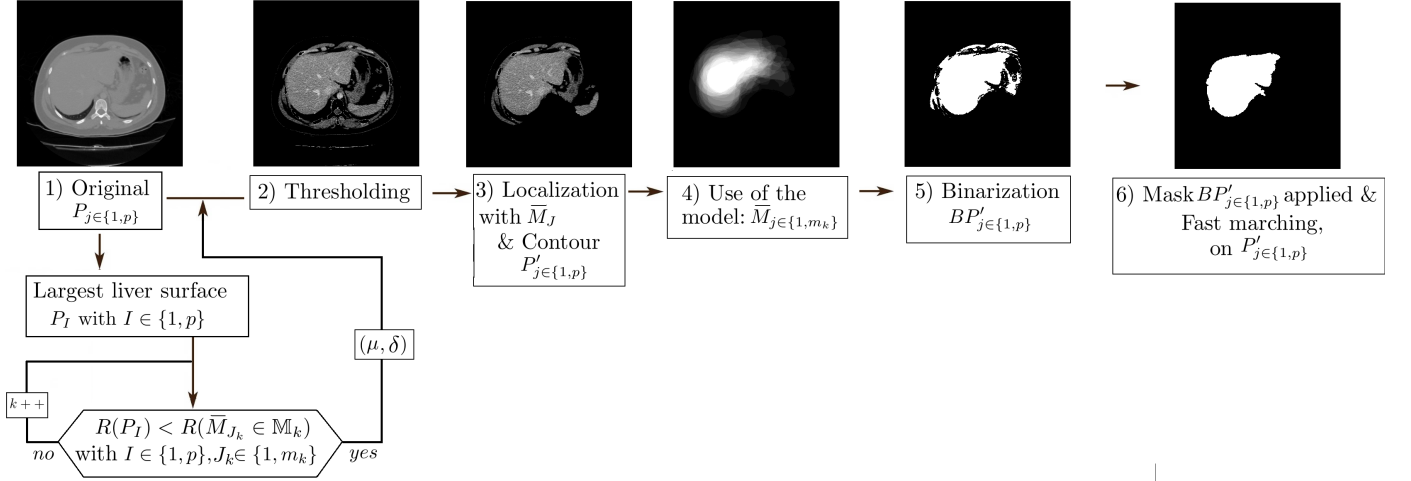


Figure 2: The complete framework for segmenting the volume of a liver

$D$  the pixel intensity distribution of  $P_I$ , with  $\mu$  its mean and  $\delta$  its standard deviation. We threshold the pixel distribution on the histogram with the following normality test:

$$\mu - \kappa(\delta)\delta \leq D \leq \mu + \kappa(\delta)\delta, \quad (5)$$

with  $\kappa(\delta) = 34.64 \times \delta^{-0.384}$ .  $\kappa(\delta)$  has a descending exponential form, that allows us to include more pixels in cases with a small value of  $\delta$  (see steps 1 and 2 in Figure 2). To limit detection of the surrounding organs, we focus our segmentation on the maximum binary area of the shape model (step 3 in Figure 2).

### 2.1.3. 3-D representation

Finally, we apply an anisotropic diffusion filter [44]. It requires three parameters: the number of iterations to be performed ( $n_{it1}$ ), the time step ( $ts$ ) and the conductance parameter ( $\xi$ ). We compute the gradient magnitude to detect the contours; the accentuated images contours are denoted by  $P'_{j \in \{1,p\}}$ . We align the shape model  $\bar{M}_{j \in \{1,m_k\}}$  with the patient data by the correspondence between  $P_I$  and  $\bar{M}_{J_k}$  (see Section 2.1.2). Then, we choose pixels with a probability higher than  $\gamma_2$  (step 4 in Figure 2). We denote the results by  $BP'_{j \in \{1,p\}}$  (step 5 in Figure 2). We apply  $BP'_{j \in \{1,p\}}$  as a mask on  $P'_{j \in \{1,p\}}$ . Finally, a fast marching method [45] is initialized with the center  $(x, y)$  of the connected component in the shape model with pixels with a probability higher than  $\gamma_2$ .

We now have a 3-D binary mask,  $MP_{j \in \{1,p\}}$ , with some segmentation errors. We use the Z-convexity property [46] of the liver shape to perform an adjustment. Let  $MP_l$ ,  $l \in \{1,p\}$ , the mask with the maximum binary area. Before  $l$ , each surface  $Surface(MP_j)$  must be included in the next one,  $Surface(MP_{j+1})$ , so pixels that do not belong to the liver are set to 0 in  $MP_j$ . After  $l$ , each surface  $Surface(MP_j)$  must be included in the previous one,  $Surface(MP_{j-1})$  (see Figure 3).

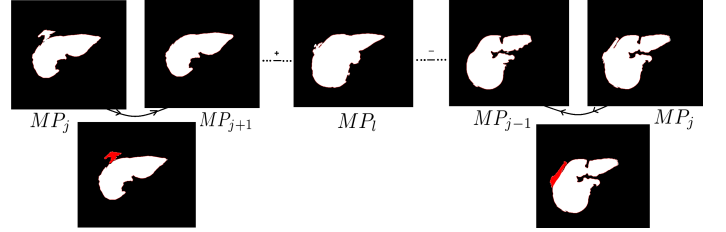


Figure 3: Adjustment to address segmentation errors. Red regions correspond to the difference between two adjacent masks due to over-segmentation

To construct a 3-D representation, we use the marching cubes algorithm [47] commonly used in medical imaging processing (see Figure 4).

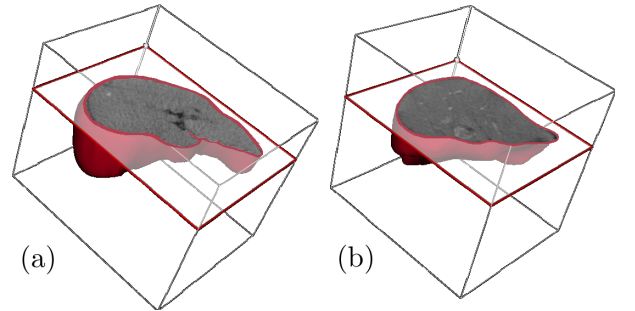


Figure 4: 3-D liver reconstructions on (a) MRI and (b) CT volumes

## 2.2. Vessels

In this section, we describe a segmentation of the main vessels of the liver delimited in the previous section on medical exams, denoted by  $I$  (see (a) in Figure 5). We extract the centerlines and reconnect the detected vessels with an iterative algorithm.

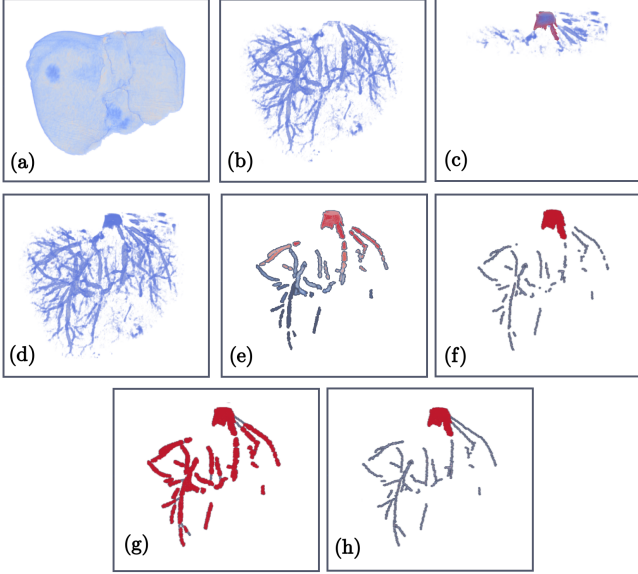


Figure 5: The complete framework for segmenting the vessels of a liver: (a) Liver segmented,  $I$ , (b) Sato's filter result,  $I_s^1$ , (c) Extraction of the confluence of the hepatic veins, (d) Result of (b) and (c), (e) Extraction of  $q$  components, (f) Centerlines extraction, (g) Centerlines extension, (h) Connection and validation

### 2.2.1. Principal components extraction

We first apply Sato's filter [23] on  $I$  with three parameters:  $\sigma$  to choose the scale of the detected structures,  $\alpha_1$  to approach the tubular similarity and  $\alpha_2$  to recover non-homogenous contrast; from this, we obtain  $I_s^1$  (see (b) in Figure 5). This filter retains many noise patterns; nonetheless, the brightest vessels are detected. The segmentation presented in Section 2.1 does not allow extraction of the confluence of the hepatic veins, which is outside the liver. To extract it, we select the largest 2-D area of the liver from among the first ten slices of  $I$  and search for the largest component (see (c) in Figure 5). Figure 5 (d) shows the first result. From this 3-D image, we extract  $q$  components  $C_{k \in \{1, q\}}$ , working from the largest to the smallest volume (see (e) in Figure 5).

### 2.2.2. Centerline extraction and extension

We extract the 3-D centerline,  $l_k$ , of each component  $C_k$  with a decision tree-based approach without user-defined parameters [48] (see (f) in Figure 5). If  $|l_k| > 1$ , we compute the direction vectors at both extremities of  $C_k$ . We call the direction at the beginning  $\mathbf{b}_k$  and at the end  $\mathbf{e}_k$  (Algorithm 1). To be in accordance with the direction, we use  $\lambda > 0$  voxels for long components and all the voxels for the shorter ones (smaller than  $\lambda$  voxels).  $l_k[j]$  is the voxel of  $l_k$  at position  $j \in \{1, n\}$  and  $n = |l_k|$  the number of voxels of  $l_k$ .

---

#### Algorithm 1 Centerline vectors

---

**Require:**  $l_k, k \in \{1, q\}$

**Ensure:**  $\mathbf{e}_k, \mathbf{b}_k, k \in \{1, q\}$

$n = |l_k|$  with  $n > 1, m = \min(n, \lambda)$

**for**  $k = 1 : p$  **do**

$\mathbf{b}_k = l_k[m] - l_k[1]$

$\mathbf{e}_k = l_k[n - m + 1] - l_k[n]$

**end for**

---

We extend the centerlines from both extremities until they reach another component and determine if a reconnection is biologically possible (see (g) in Figure 5). If  $|l_k| = 1$  ( $l_k$  has one voxel), the connection process is different because of the lack of information about its direction. We search for the four nearest (Euclidean distance) components of  $C_k$  (Figure 6).

### 2.2.3. Connection and validation

We note  $E_{k,l}$ , the extended centerline between  $C_k$  and the encountered component  $C_l$ . We evaluate the intensity  $I_s^1[i]$  with  $i \in \{1, |E_{k,l}|\}$  of each voxel of  $E_{k,l}$  in  $I_s^1$  and  $I_s^2[i]$  with  $i \in \{1, |E_{k,l}|\}$  in  $I_s^2$ .  $I_s^2$  is the result of applying Sato's filter to  $I$ , which detects larger tubular structures than parameters chosen for  $I_s^1$  (Table 3). We then compute two rates  $r_j$  with  $j \in \{1, 2\}$ :

$$r_j = \frac{\sum_{i=1}^{|E_{k,l}|} I_s^j[i]}{\max(I_s^j) \times |E_{k,l}|} \quad (6)$$

To evaluate if a connection is physically realistic, we compute the sinus of the angle  $\beta$  formed by  $E_{k,l}$  and the direction of  $C_l$  (see Figure 6 parts 2–3). If  $|l_k| > 1$  and the following condition is true, we connect the components:

$$(r_1 > t \text{ or } r_2 > t) \text{ and } (|\sin(\beta)| < \omega_1) \quad (7)$$

with  $t \in [0, 1]$  and  $\omega_1 \in [0, 1]$ . If  $C_l$  is the confluence of the hepatic veins, we directly validate the connection. In cases where  $|l_k| = 1$ , we proceed along the four lines in the same way for computation of  $r_j$ . In this last case, the candidates for the connection are ranked according to their Euclidean distance from unique voxel  $l_k$ . Then, we check the condition

$$\text{or} \left\{ \begin{array}{l} (r_1 > 2t\gamma \text{ and } r_2 > 2t\gamma) \\ (r_1 > t\gamma \text{ or } r_2 > t\gamma) \text{ and } (|\cos(\beta)| > \omega_2) \end{array} \right. \quad (8)$$

where  $\gamma$  varies in function of the distance of each component and  $\omega_2 \in [0, 1]$ . Finally, if the centerline extension is too long, values  $r_1$  and  $r_2$  can be higher than the fixed threshold due to the high number of voxels considered, so we correct using an iterative process bounded by a given maximal value  $n_{it2} > 0$ . After processing all components, we obtain an image with new principal components. At this stage, the process is re-iterated to add more connections (see (h) in Figure 5).

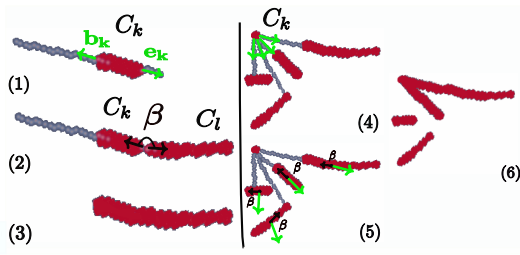


Figure 6: (1) Computation of directional vectors and centerline extension of  $C_k$  with  $|l_k| > 1$ ; (2) Evaluation of  $\beta$ , the angle between  $C_k$  and  $C_l$ ; (3) Validation of the connection; (4) Computation of the four closest components of  $C_k$  with  $|l_k| = 1$  and the directional vectors; (5) Evaluation of  $\beta$ , the angle between the directional vectors and each of four components; (6) Validation of the connections, here, a case of two validations among four possible

#### 2.2.4. 3-D reconstruction

We obtain a partial skeleton  $S_{partial}$ . We apply RORPO [28] to  $I$  to obtain  $I_R$ . RORPO uses the notion of path operators from mathematical morphology with thin voxels oriented along their length:

$$L_{n_R} = L_{min} \times f^{n_R-1}, \quad (9)$$

$L_{min}$  is the minimal path length to detect,  $f \in \mathbb{R}$  is for the geometric sequence of scales and  $n_R$  is the number of scales (Table 3). Our method uses different vesselness filters to gather different types of information about structure. Sato's filter is sensitive to different diameter ranges [23] and RORPO is based on length [28]. We decided to apply RORPO at this last step instead of using  $I$  directly because RORPO preserves the intensity of curvilinear structures, reduces the intensity of other structures, and is robust to noise. An anisotropic diffusion filter is then applied on  $I_R$  [49]. We also compute the magnitude of the gradient and use a sigmoid function to focus on a particular set of values. Finally, we initialize a fast marching phase at each voxel of  $S_{partial}$  [45] (Figure 7).

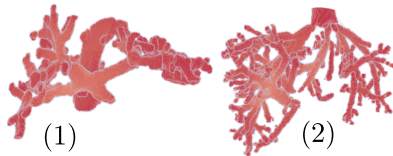


Figure 7: Our 3-D liver vessel segmentation approach applied to (1) MRI and (2) CT volumes.

### 2.3. Couinaud representation

At this stage, we have a 3-D segmentation of the liver. From this volume, derived from either MRI or CT, we extract its 3-D vascular structure. In the last step of our approach, we separate the liver into the eight functionally independent segments described by Couinaud [50].

#### 2.3.1. Segmentation of the largest vessels

To achieve this, we first erode the vessel segmentation to retrieve the largest vessels. This process allows us to erase the

smallest vessels detected in the previous section. The liver receives its blood supply from two large vessels, the portal vein and the hepatic artery. The latter carries blood from the liver to the inferior cava vein, while the first carries blood from the stomach, spleen, intestines and gallbladder to the liver. Detoxified blood leaves the liver through another large vessel, the hepatic vein. The hepatic and portal veins are not connected. After erosion, and thanks to this disconnection, we extract the two principal components, as shown on two MR images from our database in Figure 8.

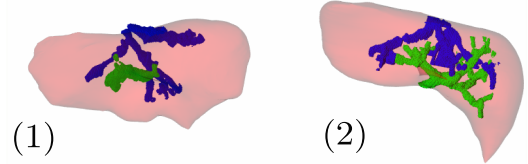


Figure 8: Results of hepatic veins (blue) and portal vein (green) extraction on MR images of patients with advanced cirrhosis.

Our method works on the livers of patients with advanced cirrhosis, as shown in Figure 8. Livers are severely deformed by cirrhosis and some other diseases; thus, segmenting vessels becomes a challenging task, because they are smaller and thinner than in a healthy liver. However, we are able to reconstruct the largest vessels, which is sufficient to construct Couinaud's scheme. Indeed, we based our method on the four main directions of the hepatic and portal veins, we explain it in the next section.

#### 2.3.2. Main directions

There are three hepatic veins in the liver, converging into an extra hepatic vein (inferior cava vein). These three directions make it possible to divide the organ vertically into a left, middle and right part. Next, the portal vein is characterized by a split into two horizontal veins that divide the liver horizontally. We want to extract these three main directions of the hepatic veins and this horizontal axis of the portal vein. After extraction of the hepatic and portal vein components in the previous section, intermediate vessels still exist; however, we seek to extract only the main direction of the largest vessels, as shown in Figure 9.

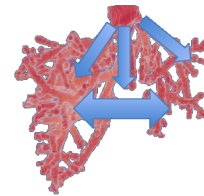


Figure 9: Main directions of the liver vascular structure on a CT scan from our database

To extract them, we proceed with two methods, one for the hepatic veins and one for the portal vein. For the hepatic veins, we keep only the first three appearances of the vessels, along the Z-axis, in a radius near the central trunk corresponding to

the beginning of the three hepatic veins. Then, we make an intersection of the 2-D binary images along the Z axis with this image (Figure 10 (a)). At the end, we obtain three oval components. We stop this process at the  $i$ -th image, which corresponds to the next division of the hepatic vessels. To compute the vectors of the three directions, we use the center of the common trunk and the center of the three components detected at the  $i$ -th image. We construct three planes with these three directions.

For the portal vein, we detect the longest horizontal component along the Z-axis (Figure 10 (b)). We compute the direction using its position along the Z-axis and the longest central axis of the component to obtain a horizontal plane.

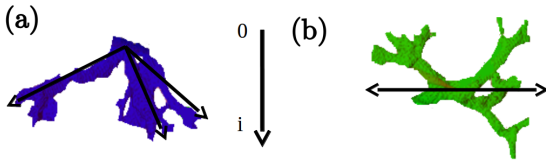


Figure 10: Extraction of the main directions of the hepatic veins (blue) and the portal vein (green) from an MRI vessel segmentation

### 2.3.3. 3-D Representation

With the four planes, we are able to divide the liver into the eight segments of the Couinaud representation. Figure 11 represents a liver segmentation performed with our automatic algorithm presented in Section 2.1, and the four planes constructed from the vascular segmentation presented in Section 2.2.

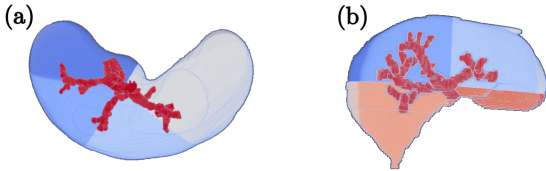


Figure 11: Couinaud representation of MRI volumes (a) Left, middle and right part of the liver delimited by the three hepatic veins, (b) Upper and lower part of the liver delimited by the portal vein. Illustration was created from an MRI from our database of a liver from a patient with advanced cirrhosis.

## 3. Results

In the first part of this section, we evaluate our complete automatic framework by applying it to both CT and MRI. We first evaluate the segmentation of the liver presented in Section 2.1 by comparison with other semi-automatic and automatic methods. Then, we present results of the vessel segmentation presented in Section 2.2. Finally, we present a new method to measure the accuracy of the Couinaud segmentation. The steps of our method can be viewed in a video <sup>1</sup>. We implemented all algorithms with ITK-VTK [51, 52].

<sup>1</sup><https://youtu.be/FNN6Yo5qxbQ>

### 3.1. Data and parameters

To evaluate our automatic method, we use CT images from two freely available databases: 20 from the SLIVER database [43] and 20 from the IRCAD database [42]. Both databases are widely used in research because some manual segmentations (of liver or/and vessels) are available and they are, therefore, directly comparable. We do not use Shape 2015 database, here, because medical examinations are not available in this dataset. Then, during the shape model construction (see Section 2.1), some of those testing data are used. To avoid bias, each of the set used in the shape model chosen are removed. The image sizes are  $512 \times 512 \times 64$ - $394$ , with a voxel size of  $0.56$ - $0.87 \times 0.56$ - $0.87 \times 0.7$ - $5 \text{ mm}^3$ .

We also use 40 MRI volumes from different local hospitals (CHU Clermont Ferrand, France and CH Emile Roux, France). Image sizes are  $250 - 512 \times 320 - 512 \times 56$ - $112$ , with a voxel size of  $0.82$ - $1.40 \times 0.82$ - $1.40 \times 1.8$ - $3 \text{ mm}^3$ . The 40 liver images in our MRI database come from patients with diseases such as advanced cirrhosis and cancers (including hepatocellular carcinoma). In these cases, segmentations are a challenging task, because the image quality decreases considerably with more heterogeneous liver tissue density; moreover, as mentioned above, livers are severely deformed by the progression of these diseases and there is a decrease in the liver-vessel contrast. Parameters used in the method described in Section 2 are presented in Table 3.

Liver parameters	$n_{it1}$	$ts$	$\xi$	$\gamma_1$ (%)	$\gamma_2$ (%)
	5	0.1	1	30	30
Vessel Parameters	$q$	$\lambda$	$t$	$n_{it2}$	$\omega_1, \omega_2$
Sato $I_s^1$	$\sigma$	$\alpha_1$	$\alpha_2$		
	2	0.1	0.9		
Sato $I_s^2$	$\sigma$	$\alpha_1$	$\alpha_2$		
	2	3	0.9		
RORPO $I_R$	$L_{min}$	$f$	$n_R$		
	40	1.32	4		

Table 3: Fixed parameters used to segment the liver in Section 2.1 and vessels in Section 2.2, listed with their corresponding values.

Some parameters are chosen based on the literature, including those for RORPO [28], and Sato's filter [23]. Others were derived from the anisotropic diffusion filter in the liver segmentation ( $n_{it1}$ ,  $ts$ ,  $\xi$ ). We have modified the conductance  $\xi$  to adapt the process to our dataset. Then, some parameters are determined empirically. These parameters are sufficiently generic to work with all images, like  $t$ , that allows us to consider intensity values on the results of the Sato's filters;  $\omega_1$  and  $\omega_2$ , which reflect a connection between two vessels close to a right angle; and  $n_{it2}$ , which limits the size of the centerline extension. We spent time manually optimizing other parameters, like the percentages  $\gamma_1$  and  $\gamma_2$  in the liver segmentation; the number of components  $q$  to be detected, and the direction of the component  $\lambda$  in the vessel segmentation. In the future we may consider developing automatic calculation processes to pick the best parameters (optimization) using training datasets.

### 3.2. Liver results

Manual segmentations of the liver are available for the CT images from SLIVER and IRCAD, and our experts segmented livers on three MRI volumes. Quantitative results are presented in Table 4. Our automatic method and experts’ manual segmentations of the liver are compared by widely used metrics designed to quantify accuracy. We use True Positive (TP) and False Negative (FN) rates in the range 0–1 to evaluate the RE-call value (RE), the PREcision value (PRE), the Jaccard index (J) and the Dice coefficient (D).

Dataset	RE	J	D
IRCAD	0.87±0.05	0.78±0.06	0.88±0.03
SLIVER	0.92±0.03	0.87±0.04	0.93±0.02
MRI	0.91±0.08	0.82±0.04	0.90±0.02
	FN	TP	PRE
IRCAD	0.13±0.05	0.85±0.07	0.89±0.04
SLIVER	0.8±0.03	0.92±0.03	0.94±0.03
MRI	0.9±0.07	0.90±0.10	0.88±0.06

Table 4: Liver segmentation accuracy on CT and MRI volumes

We now compare our method with automatic algorithms based on statistical models. Massoptier *et al.* [13] report a superior Dice coefficient of 0.94. The similarity of our model is not as high as theirs, but it is close, and offers a time advantage: their method requires 11.4 seconds for processing a  $512 \times 512$ -pixel slice, while ours requires only 5–6 s. For purposes of comparison, a manual expert segmentation generally requires 180–240 s for one slice [53]. Okada *et al.* [18] obtain a Jaccard coefficient of 0.86 for 8 CT scans; we obtain 0.87 for the 20 SLIVER images. Farzaneh *et al.* [14] obtain a Dice coefficient higher than 0.89 on 11 similar images in pixel spacing. The mean Dice value in our study is 0.905 for 40 different datasets.

Then, we compare our method with the results of efficient liver segmentations applied to the IRCAD and SLIVER datasets. Linguraru *et al.* [15] present an automatic method with a 0.96 Dice value for the SLIVER database, but their atlas-based method requires 3000–3600 s per slice. Our results do not perform as well as methods described in [11, 16, 19, 54, 55]; however, all of these studies concentrate their task only on CT scans. Moreover, the process presented by Yang *et al.* [11] is user-dependent. The advantage of our methodology is that it is automatic, generic, and works on both CT and MRI volumes with promising results.

Few studies have reported results for both modalities; we compare our results with those of the most recent studies to do so [56, 57, 58, 59]. The performance of our method is similar to the other reported methods, but ours offers some advantages; for example, methods presented by Gotra *et al.* [56], Chartrand *et al.* [57] and Suzuki *et al.* [58] are user-dependent, while ours is automatic. Moreover, in one study [56], the same patients were used for CT and MRI, which limits the variability of the data and the range of liver shapes. Finally, our results are better than those obtained by Heinrich *et al.* [59], see Table 5, who present an atlas for registration of CT and MRI data.

Method, Ref	CT			MRI		
	Data	D	J	Data	D	J
Auto, ours	SLIVER	0.93	0.87	private	0.90	0.87
	IRCAD	0.88	0.78			
Semi-Auto, [58] 2015	private	0.93		private	0.93	
Semi-Auto, [56] 2017	private		0.90	private		0.88
Semi-Auto, [57] 2017	SLIVER		0.94	private		0.92
Auto, [59] 2015	private	0.92		private	0.80	

Table 5: Comparison with other methods on CT and MRI volumes

### 3.3. Vessel segmentation results

We first evaluate our method presented in Section 2.2 on 10 synthetic vascular images from the March 2013 VascuSynth database used by Cheng *et al.* [60]. Averages with standard deviations of True Positives (TP), False Positives (FP), False Negatives (FN) and Overlap Measure (OM) [60] are reported in Table 6. We do not have false positives in our results, because our method of extraction of the main components and our partial skeletonization process efficiently handles synthetic data without noise. Moreover, RORPO is an efficient algorithm for the enhancement of vascular structures.

	FN	FP	TP	OM
[60]	3.63 ± 1.05	5.95 ± 1.37	96.37 ± 1.05	95.78 ± 1.23
Ours	2.41 ± 1.99	0	97.58 ± 1.1	98.77 ± 1.03

Table 6: Segmentation results of our method on synthetic vascular images (March 2013 VascuSynth database)

Our algorithm has better results than those of article [60] for these specified criteria.

Then, we apply our vessel segmentation on CT images from the public IRCAD database [42]. In this database, different contrast agents are used and therefore different levels of contrast enhancement are present. IRCAD offers manual segmentation sets {artery, portal vein, venous system, vena cava}, which allow for further comparison with other methods. Unfortunately, most of the methods described in the literature were tested using private databases, and did not publish their code, making retrospective comparative studies impossible [25, 27, 34].

As far as we know, there are no open MRI datasets available for liver vessels. A medical expert working with us has segmented portal and hepatic veins for an MRI volume at the portal and arterial phases (times after contrast agent injection), when vessels are most visible. Using these data we quantitatively compare our method with RORPO and Sato’s filter (which were thresholded beforehand) based on several classic metrics: accuracy (ACC), specificity (SPE), sensitivity (SENS) and precision (PRE). To measure misclassification, we also compute the false positive and negative rates (FPR, FNR). The FPR represents the degree of over-segmentation and the FNR the under-segmentation. We only evaluate these metrics on the area delimited by the liver segmentation presented in Section 2.1.

CT	ACC	SPE	SENS	PRE	FPR	FNR
Ours	0.97±0.01	0.98±0.01	0.69±0.10	0.61±0.07	0.01±0.01	0.32±0.09
RORPO	0.90±0.02	0.97±0.01	0.20±0.06	0.41±0.09	0.02±0.01	0.80±0.06
Sato	0.89±0.03	0.97±0.02	0.24±0.10	0.46±0.17	0.03±0.01	0.75±0.10
MRI	ACC	SPE	SENS	PRE	FPR	FNR
Ours (hepatic)	0.98	0.98	0.54	0.30	0.010	0.45
Ours (portal)	0.97	0.98	0.70	0.51	0.002	0.32
RORPO (hepatic)	0.96	0.98	0.23	0.30	0.016	0.78
RORPO (portal)	0.98	0.99	0.56	0.46	0.007	0.43
Sato (hepatic)	0.97	0.97	0.39	0.27	0.012	0.60
Sato (portal)	0.97	0.90	0.10	0.39	0.030	0.90

Table 7: Results of our automatic algorithm to segment vessels on CT and MRI.

The accuracy, sensitivity and precision values for CT and sensitivity and precision values for MRI suggest that our method is more accurate than other tested methods, see Table 7. The principal components are well-distributed in the liver; however, the detection step fails in places where large vessels are not present, explaining the high FNR results. Moreover, noise is present in the manual MRI segmentation because of the software used by the expert. In addition, the image quality decreases because we are quantitating diseased liver tissue.

### 3.4. Couinaud segmentation results

We present here a new process to evaluate the Couinaud representation. We use MR images,  $MRI_i$  with  $i \in \{1, 4\}$ , from our database for which an expert validated our visual results, and CT scans,  $CT_i$  with  $i \in \{1, 8\}$  from the IRCAD database. Among these four MRI volumes, some of the imaged livers have cirrhosis too advanced (with the presence of tumors in many segments) to allow for surgical planning. The Couinaud scheme is useful for localized, resectable tumors; as explained in Section 2.3, it uses the horizontal portal vein orientation and the three vertical hepatic veins axes to divide the liver into eight functionally independent segments (see Figure 1). Vessel segmentation explained in Section 2.2 allows us to construct this representation. This segmentation is used in daily clinical practice to indicate the exact positions of tumors, which is of high interest in surgical planning.

In the state-of-the-art, evaluation of Couinaud segmentation is done by volumetric validation [36, 38]; by graft volumetry accuracy and visual comparison [61]; or solely by visual comparison [30]. In our study, we evaluate the Couinaud scheme relative to tumors' positions as presented in medical reports by hospital staff.

Patient	Segments: Tumors' positions (medical reports)	Number of tumors found with correct position
$MRI_1$	1 in {VII}	1
$MRI_2$	1 in {VIII} and 1 at {V, VI, VII}	2
$MRI_3$	1 in {IV} and 1 in {VIII}	2
$MRI_4$	2 in {III}	2
$CT_1$	1 in {III}, 1 in {IV, V} 1 in {VII} and 1 in {VIII}	3 (missed 1 in {III})
$CT_2$	1 in {V, VIII}	1
$CT_3$	1 in {I}, 1 in {II} and 1 in {IV}	3
$CT_4$	1 in {IV, II}	1
$CT_5$	1 in {V}	1

Table 8: Validation of tumor position in the Couinaud segmentation based on medical reports

MRI is a very effective medical imaging tools for many purposes, including the early detection of primary liver cancer, metastases and characterization of hepatic nodules, and it is the main modality used for this purpose by the experts we consulted. For each patient, we have access to two or three reports that correspond to different examination dates, which allows us to confirm the evolution of tumors' positions. We also evaluate our Couinaud segmentation by comparison with CT scans of livers with advanced cirrhosis.

Some large tumors can be observed in different segments, as seen for  $MRI_2$  and  $CT_1$  for segments {V, VI, VII} and {IV, V} respectively in Table 8. We observe that tumors appear in the positions indicated in the patients' medical reports, confirmed by our Couinaud segmentation with a large variety of localization within liver (see examples in Figure 12 (a) and (b)). However, our method fails for  $CT_1$  to detect the tumor in the segment {III}, instead the lesion is found in segment {IV}; one of the Couinaud axes (in red in the Figure 12 (c)) is false because of a wrong detection of the hepatic vein. For two volumes,  $CT_6$  and  $CT_7$ , the tumors occupy the whole liver, despite this condition the algorithm is efficient. It also works on the healthy liver in  $CT_8$  that has no tumors. Couinaud segmentation is sensitive to the state of health of the liver, because livers are deformed by the progression of cirrhosis.

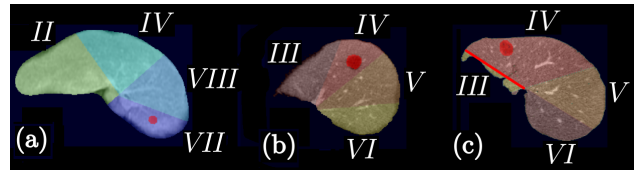


Figure 12: Tumors found in red with correct position: (a) segment {VII} for  $MRI_1$  (b) segment IV for  $CT_3$ ; (c) Our method fails for  $CT_1$ : the tumor is found in segment {IV} instead of in the segment {III}. The red axis has been incorrectly calculated.

## 4. Discussion

In this article, we present a complete method to segment the liver and its vessels to obtain the Couinaud representation. Our algorithms are automatic and work on CT and MRI images obtained from different machines and acquisition parameters. First, we are able to automatically segment the liver using a model-based method that takes into account the variability in liver shape. This method can be used to process any medical image by overcoming the parametric constraints imposed by the machines and leads to a 3-D reconstruction for CT and MRI volumes. Few studies have reported results for both modalities [56, 57, 58, 59]. Among them, we outperform the automatic method [59]; the others require user interaction. We obtain a mean Dice coefficient of 0.915 for all volumes across both modalities. Our method is efficient even in the case of advanced cirrhosis with a dysmorphic liver, these studies do not all describe results for diseased livers. From our liver segmentation, we propose an automatic 3-D vessel segmentation based on an iterative partial skeletonization process. There are few methods that combine tubular objects in connected networks via skeletonization [34, 35], it's an originality of our work. We present

this concept combined with the use of a partial skeletonization process. Even though the analysis can be complex due to the severity of the pathology, we are able to segment enough vessels to correctly extract the vessels.

Our method is also efficient on CT and MR images, even images of livers with thinner vessels due to advanced disease, with a mean accuracy equal to 0.97; for more on this result, see [62]. Finally, we extract the main directions of the largest vessels, the hepatic and portal veins, in order to construct the Couinaud representation. Evaluation of the scheme is usually done by volumetric validation or visual comparison [38, 36, 61, 30]; in this study, we present an evaluation based on medical reports. As this representation is used for the location and resection of tumors, it is useful to evaluate it through these tumors' positions. In future work, this representation of Couinaud can be improved by considering curved surfaces instead of straight planes to cut the segments.

For the execution time, we specified that it took 5-6 seconds for a  $512 * 512$  image for the liver segmentation. To segment the vascular structure, it takes 8 minutes for a 3-D volume; the 3-D ITK algorithm to find the centerlines implies a long time. As a future work, we could use another algorithm to speed up the complete pipeline. The execution time for tumors detection is presented by Pavan *et al.*[63], it depends on image patch size and number of processors used in our parallel approach. The best time is 5 sec. for a single patient (with 16 processors).

The method outlined in this paper has some limitations. First, we need to improve the different planes of the Couinaud segmentation in order to improve accuracy in the process of detecting tumors. Second, vessel segmentation and the detection of the hepatic and portal veins are based on location of the largest vessels. However, when the patient has advanced cirrhosis, the vessels are atrophied and our method may fail. Finally, we need more data to test the vessel segmentation, the Couinaud classification and to quantify the level of deformities acceptable by our algorithms. To become part of the clinical routine, the algorithm must be faster. Therefore, improvement of the (currently slow) centerline extraction algorithm will be necessary.

## 5. Conclusion

Our contributions are multiple. First, the algorithm is multi-modal, it can handle both computed tomography and MRI. Then, it is automatic from the segmentation of the liver to the Couinaud division. We propose a complete framework whatever the modalities used. Finally, we propose an evaluation of our Couinaud scheme that goes beyond the simple visual inspection, as in similar studies. Our approach is easy-to-implement and can be easily deployable for a clinical way.

In the future, we will add comparisons with skeletonisation process, evaluate more results from MRI data, and create standard annotations for benchmarking. We are currently working with different MRI acquisition times (portal, arterial, diffusion, *etc.*). We employ 3-D reconstructions of these dynamic MRI volumes to develop a method for automatic tumor detection, as radiologists do with visual criteria based on the different acquisition times; the Couinaud representation serves as the validation step. Thanks to these complete 3-D segmentations, we are

already able to detect hepatic tumors such as hepatocellular carcinoma [63], and to study blood flow in order to locate the onset of possible dysfunctions [64].

## References

- [1] Liver segment classification by Couinaud, by Was a bee, is licensed by CC-BY-SA-2.1-JP, [https://commons.wikimedia.org/wiki/File:Liver/.04.Couinaud\\_classification\\_animation.gif](https://commons.wikimedia.org/wiki/File:Liver/.04.Couinaud_classification_animation.gif), accessed in 2019.
- [2] J. Peng, F. Dong, Y. Chen, D. Kong, A region-appearance-based adaptive variational model for 3-D liver segmentation, *Medical physics* (2014) 41 (4).
- [3] L. Ruskó, G. Bekes, M. Fidrich, Automatic segmentation of the liver from multi- and single-phase contrast-enhanced CT images, *Medical Image Analysis* 13 (6) (2009) 871–882.
- [4] R. Yuan, M. Luo, S. Wang, L. Wang, Q. Xie, A method for automatic liver segmentation from multi-phase contrast-enhanced CT images, *Medical Imaging: Computer-Aided Diagnosis* 9035 (2014) 90353H.
- [5] A. H. Foruzan, R. Aghaeizadeh Zoroofi, M. Hori, Y. Sato, Liver segmentation by intensity analysis and anatomical information in multi-slice CT images, *International Journal of Computer Assisted Radiology and Surgery* 4 (3) (2009) 287–297.
- [6] S. J. Lim, Y. Y. Jeong, Y. S. Ho, Automatic liver segmentation for volume measurement in CT Images, *Journal of Visual Communication and Image Representation* 17 (4) (2006) 860–875.
- [7] P. Campadelli, E. Casiraghi, S. Pratisoli, G. Lombardi, Automatic abdominal organ segmentation from CT images, *ELCVIA: Electronic Letters on Computer Vision and Image Analysis* 8 (1) (2009) 1–14.
- [8] C. Shi, Y. Cheng, F. Liu, Y. Wang, J. Bai, S. Tamura, A hierarchical local region-based sparse shape composition for liver segmentation in CT scans, *Pattern Recognition* 50 (2016) 88–106.
- [9] F. Liu, B. Zhao, P. K. Kijewski, Liver segmentation for CT images using GVF snake, *Medical physics* 32 (12) (2005) 3699–3706.
- [10] L. Soler, H. Delingette, G. Malandain, J. Montagnat, N. Ayache, C. Koehl, O. Dourthe, B. Malassagne, M. Smith, D. Mutter, J. Marescaux, Fully automatic anatomical, pathological, and functional segmentation from CT scans for hepatic surgery, *Computer Aided Surgery* 6 (3) (2001) 131–142.
- [11] X. Yang, H. C. Yu, Y. Choi, W. Lee, B. Wang, J. Yang, H. Hwang, J. H. Kim, J. Song, B. H. Cho, H. You, A hybrid semi-automatic method for liver segmentation based on level-set methods using multiple seed points, *Computer Methods and Programs in Biomedicine* 113 (1) (2014) 69–79.
- [12] A. Brunton, A. Salazar, T. Bolkart, S. Wuhler, C. Hau Chen, Statistical shape spaces for 3-D data: a review, *Handbook of Pattern Recognition and Computer Vision* (2016) 978–981.
- [13] L. Massotier, S. Casciaro, A new fully automatic and robust algorithm for fast segmentation of liver tissue and tumors from CT scans, *European radiology* (2008) 1658–1665.
- [14] N. Farzaneh, S. Samavi, S. R. Sorousmehr, H. Patel, S. Habbo-Gavin, D. P. Fessell, K. R. Ward, K. Najarian, Liver segmentation using location and intensity probabilistic atlases, *IEEE International Engineering in Medicine and Biology Conference (EMBC)* (2016) 6453–6456.
- [15] M. G. Linguraru, J. K. Sandberg, Z. Li, F. Shah, R. M. Summers, M. G. Linguraru, J. K. Sandberg, Z. Li, Automated segmentation and quantification of liver and spleen from CT images using normalized probabilistic atlases and enhancement estimation, *Medical physics* 771 (2010).
- [16] C. Shi, Y. Cheng, J. Wang, Y. Wang, K. Mori, S. Tamura, Low-rank and sparse decomposition based shape model and probabilistic atlas for automatic pathological organ segmentation, *Medical Image Analysis* 38 (2017) 30–49.
- [17] B. He, C. Huang, G. Sharp, S. Zhou, Q. Hu, C. Fang, Y. Fan, F. Jia, Fast automatic 3-D liver segmentation based on a three-level AdaBoost-guided active shape model, *Medical Physics* 43 (5) (2016) 2421.
- [18] T. Okada, R. Shimada, Y. Sato, M. Hori, K. Yokota, M. Nakamoto, Y.-W. Chen, H. Nakamura, S. Tamura, Automated segmentation of the liver from 3-D CT images using probabilistic atlas and multi-level statistical shape model, *International Conference On Medical Image Computing and Computer Assisted Intervention, MICCAI* 10 (2007) 86–93.
- [19] J. Wang, Y. Cheng, C. Guo, Y. Wang, S. Tamura, Shape-intensity prior level set combining probabilistic atlas and probability map constrains for

- automatic liver segmentation from abdominal CT images, *International Journal Computer Assisted Radiology and Surgery* 11 (5) (2016) 817.
- [20] T. F. Cootes, C. J. Taylor, Statistical models of appearance for medical image analysis and computer vision, *International Society for Optics and Photonics* 4322 (236-248) (2001) 236.
- [21] T. F. Cootes, G. J. Edwards, C. J. Taylor, Others, Comparing active shape models with active appearance models, *British Machine Vision Conference* 99 (1) (1999) 173–182.
- [22] A. F. Frangi, W. J. Niessen, K. L. Vincken, M. A. Viergever, Multiscale vessel enhancement filtering, *International Conference On Medical Image Computing and Computer Assisted Intervention, MICCAI* (1998) 130.
- [23] S. N. Yoshinobu Sato, 3-D Multi-scale line filter for segmentation and visualization of curvilinear structures in medical images, *CVRMed-MRCAS* (1997) 213–222.
- [24] M. Erdt, M. Raspe, M. Suehling, Automatic hepatic vessel segmentation using graphics hardware, *Medical Imaging and Augmented Reality* 20 (1) (2000) 403–412.
- [25] F. Conversano, R. Franchini, C. Demitri, L. Massoptier, F. Montagna, A. Maffezzoli, A. Malvasi, S. Casciaro, Hepatic vessel segmentation for 3-D planning of liver surgery: experimental evaluation of a new fully automatic algorithm, *Academic radiology* 18 (4) (2011) 461–470.
- [26] M. Marcan, D. Pavliha, M. M. Music, I. Fuckan, R. Magjarevic, D. Miklavcic, Segmentation of hepatic vessels from MRI images for planning of electroporation-based treatments in the liver, *Radiology and Oncology* 48 (3) (2014) 267–281.
- [27] Y. Z. Zeng, Y. Q. Zhao, M. Liao, B. J. Zou, X. F. Wang, W. Wang, Liver vessel segmentation based on extreme learning machine, *Journal of the Italian Association of Biomedical Physics (AIFB)* 32 (5) (2016) 709–716.
- [28] O. Merveille, H. Talbot, L. Najman, N. Passat, Curvilinear structure analysis by ranking the orientation responses of path operators, *IEEE TPAMI* (2018) 40.
- [29] N. Passat, S. Salmon, J.-P. Armspach, B. Naegel, C. Prud’Homme, H. Talbot, A. Fortin, S. Garnotel, Others, From Real MRA to Virtual MRA: Towards an Open-Source Framework, *International Conference On Medical Image Computing and Computer Assisted Intervention, MICCAI 9902* (2016) 335–343.
- [30] D. A. Oliveira, R. Q. Feitosa, M. M. Correia, Segmentation of liver, its vessels and lesions from CT images for surgical planning, *BioMedical Engineering Online* (2011) 10 (1).
- [31] S. Lu, H. Huang, P. Liang, G. Chen, L. Xiao, Hepatic vessel segmentation using variational level set combined with non-local robust statistics, *Magnetic Resonance Imaging* 36 (2017) 180–186.
- [32] O. Wink, W. J. Niessen, M. A. Viergever, Multiscale vessel tracking, *IEEE T-MI* 23 (1) (2004) 130–133.
- [33] M. Schneider, S. Hirsch, B. Weber, G. Székely, B. H. Menze, Joint 3-D vessel segmentation and centerline extraction using oblique Hough forests with steerable filters, *Medical Image Analysis* 19 (1) (2015) 220–249.
- [34] C. Bauer, T. Pock, E. Sorantin, H. Bischof, R. Beichel, Segmentation of interwoven 3-D tubular tree structures utilizing shape priors and graph cuts, *Medical Image Analysis* 14 (2) (2010) 172–184.
- [35] T. Pock, C. Janko, R. Beichel, H. Bischof, Multiscale medialness for robust segmentation of 3-D tubular structures, *Proceedings of the Computer Vision Winter Workshop* (2005) 2005.
- [36] Y. Chen, X. Yue, C. Zhong, G. Wang, Functional region annotation of liver ct image based on vascular tree, *BioMed* (2016).
- [37] D. Selle, B. Preim, A. Schenk, H. O. Peitgen, Analysis of vasculature for liver surgical planning, *IEEE T-MI* 21 (11) (2002) 1344–1357.
- [38] S. H. Huang, B. L. Wang, M. Cheng, W. L. Wu, X. Y. Huang, Y. Ju, A fast method to segment the liver according to Couinaud’s classification, *Medical imaging and informatics* 4987 (2008) 270–276.
- [39] L. Soler, S. Nicolau, P. Pessaux, D. Mutter, J. Marescaux, Real-time 3-D image reconstruction guidance in liver resection surgery, *Hepatobiliary surgery and nutrition* 3 (2) (2014) 73–81.
- [40] X. Zhao, M. Huang, Q. Zhu, T. Wang, Q. Liu, The relationship between liver function and liver parenchymal contrast enhancement on gd-bopta-enhanced mr imaging in the hepatocyte phase, *Magnetic resonance imaging* 33 (6) (2015) 768–773.
- [41] M. Kistler, S. Bonaretti, M. Pfahrer, R. Niklaus, P. Büchler, The virtual skeleton database: An open access repository for biomedical research and collaboration, *Journal of Medical Internet Research* 15 (2013) (11).
- [42] <http://www.ircad.fr/research/3d-ircadb-01/>, (2018).
- [43] T. Heimann, Comparison and evaluation of methods for liver segmentation from CT datasets, *IEEE Transactions on Medical Imaging*, 28 (8) (2009) 1251–1265.
- [44] A. Draoua, A. Albouy-Kissi, A. Vacavant, V. Sauvage, A new iterative method for liver segmentation from perfusion CT scans, *International Society for Optics and Photonics* 9037 (2014).
- [45] J. A. Sethian, Level set methods and fast marching methods: evolving interfaces in computational geometry, fluid mechanics, compute vision, and materials science, Cambridge University Press (1999).
- [46] C. E. Kim, Digital straight lines and convexity of digital regions, *IEEE TPAMI* (1982).
- [47] W. E. L. Cline, Marching cubes: A high resolution 3-D surface construction algorithm, *International Conference on Computer Graphics and Interactive Techniques* 21 (4) (1987) 163–169.
- [48] H. Homann, Implementation of a 3-D thinning algorithm, *Insight-Journal* 421 (2007) 4–7.
- [49] R. Whitaker, Variable-conductance, level-set curvature for image denoising, *International Conference on Image Processing* 2 (2001) 142–145.
- [50] C. Couinaud, *Le foie: études anatomiques et chirurgicales*, Masson & Cie, (1957).
- [51] T. S. Yoo, M. J. Ackerman, W. E. Lorensen, W. Schroeder, V. Chalana, S. Aylward, D. Metaxas, R. Whitaker, Engineering and algorithm design for an image processing API: a technical report on ITK—the Insight Toolkit, *Studies in health technology and informatics* 85 (2002) 586–92.
- [52] W. J. Schroeder, B. Lorensen, K. Martin, *The visualization toolkit* (2006).
- [53] L. Hermoye, I. Laamari-Azjal, Z. Cao, L. Annet, J. Lerut, B. M. Dawant, B. E. Van Beers, Liver segmentation in living liver transplant donors: comparison of semi-automatic and manual methods, *Radiology* 234 (1) (2005) 171–178.
- [54] A. Wimmer, J. Hornegger, G. Soza, Implicit active shape model employing boundary classifier, *19th International Conference on Pattern Recognition* (2008) 1–4.
- [55] M. Moghbel, S. Mashohor, R. Mahmud, M. Iqbal, B. Saripan, Automatic liver tumor segmentation on computed tomography for patient treatment planning and monitoring, *EXCLI Journal* 15 (2016) 406–423.
- [56] A. Gotra, G. Chartrand, K. N. Vu, F. Vandenbroucke-Menu, K. Massicotte-Tisluck, J. A. de Guise, A. Tang, Comparison of MRI- and CT-based semi-automated liver segmentation: a validation study, *Abdominal Radiology* 42 (2) (2017) 478–489.
- [57] G. Chartrand, T. Cresson, R. Chav, A. Gotra, A. Tang, J. A. De Guise, Liver segmentation on CT and MR using laplacian mesh optimization, *IEEE Transactions on Biomedical Engineering* 64 (9) (2017) 2110–2121.
- [58] K. Suzuki, H. T. Huynh, Y. Liu, D. Calabrese, K. Zhou, A. Oto, M. Hori, Computerized segmentation of liver in hepatic CT and MRI by means of level-set geodesic active contouring, *IEEE International Engineering in Medicine and Biology Conference (EMBC)* (2013) 2984–2987.
- [59] M. P. Heinrich, O. Maier, H. Handels, Multi-modal multi-atlas segmentation using discrete optimisation and self-similarities, *VISCERAL Challenge@ ISBI* (2015).
- [60] Y. Cheng, X. Hu, J. Wang, Y. Wang, S. Tamura, Accurate vessel segmentation with constrained B-snake, *IEEE TIP* 24 (8) (2015) 2440–2455.
- [61] X. Yang, J. D. Yang, H. P. Hwang, H. C. Yu, S. Ahn, B. W. Kim, H. You, Segmentation of liver and vessels from CT images and classification of liver segments for preoperative liver surgical planning in living donor liver transplantation, *Computer Methods and Programs in Biomedicine* 158 (2018) 41–52.
- [62] M.-A. Lebre, A. Vacavant, M. Grand-Brochier, O. Merveille, P. Chabrot, A. Abergel, B. Magnin, Automatic 3-D skeleton-based segmentation of liver vessels from MRI and CT for Couinaud representation, *IEEE International Conference on Image Processing* (2018) 3523–3527.
- [63] A. Pavan, M. Benabdallah, M. Lebre, A. Pina, Diana Rodrigues, A. Vacavant, A parallel framework for HCC detection in DCE-MRI sequences with wavelet-based description and SVM classification, *Proceedings of the 33rd Annual ACM SAC* (2018) 14–21.
- [64] M.-A. Lebre, K. Arrouk, A.-K. Vø Vn, A. Leborgne, M. Grand-Brochier, P. Beaupaire, A. Vacavant, B. Magnin, A. Abergel, P. Chabrot, Medical image processing and numerical simulation for digital hepatic Parenchymal Blood Flow, Simulation and Synthesis in Medical Imaging, workshop of International Conference On Medical Image Computing and Computer Assisted Intervention, MICCAI (2017) 99–108.